MATERIALS CHEMISTRY FRONTIERS

RESEARCH ARTICLE

View Article Online
View Journal | View Issue

Cite this: *Mater. Chem. Front.*, 2025, **9**, 1906

Molecular engineering-facilitated AIE-active type-I photosensitizers for photothermal imaging-guided photodynamic therapy†

Xiufeng Li, Shasha Zhang, Pengli Gu, Xinyi Zhang and Ju Mei *

Despite its multiple advantages, the application of fluorescence imaging-guided photodynamic therapy based on type-II photosensitizers is still restricted by the autofluorescence of organisms and the hypoxic microenvironment of tumors. Optical agents with photothermal imaging ability and radical-based type-I reactive oxygen species (ROS) generation capability, which are exempted from the autofluorescence interference and hypoxia limitation, are thus highly desirable. In this study, we propose a molecular engineering strategy based on electron donor (D)–acceptor (A) systems, which promotes the photothermal conversion as well as the generation of type I ROS by manipulating the electron-donating and electron-withdrawing groups to boost the intersystem crossing and enhance nonradiative decay. Among the four designed D–A conjugated molecules, TPACzPy, composed of electron-donating 9-ethyl-*N*,*N*-bis-(4-methoxyphenyl)-9*H*-carbazol-2-amine, π-bridging (2*Z*,2′*Z*)-2,2′-(1,4-phenylene)bis(but-2-enenitrile), and electron-withdrawing 1-ethylpyridin-1-ium, exhibits the best comprehensive performance. This compound was thus prepared into biocompatible nanoparticles *via* a nanoprecipitation method with Pluronic F-127 as the encapsulation matrix. The photothermal performance under 660 nm-laser irradiation and the type I photosensitizing properties under white-light irradiation enable the photothermal imaging-guided photodynamic therapy of 4T1 tumors by the TPACzPy nanoparticles, demonstrating the potential of TPACzPy to be applied in cancer diagnosis and inhibition of tumors.

Received 30th January 2025,
Accepted 17th April 2025

DOI: 10.1039/d5qm00094g

rsc.li/frontiers-materials

Introduction

Currently, cancer remains one of the leading causes of human death.[1–4] Traditional therapies such as surgery, chemotherapy, and radiotherapy have achieved great success in cancer treatment. However, their challenges including invasiveness, unignorable side effects, and relatively poor therapeutic effect still trouble patients.[3,5–7] In recent years, phototheranostics have garnered widespread interest in cancer treatment because of their capacity to diagnose in real-time and treat *in situ* by virtue of optical agents which possess both imaging and therapeutic capabilities.[3,8–10] Fluorescence imaging (FLI) is the most common diagnostic imaging modality. Nevertheless, FLI has restrictions of limited tissue penetration and unavoidable background fluorescence.[4] By contrast, photothermal imaging (PTI) offers deeper tissue penetration, lower background noise, and more accurate thermal signals of the focal area.[10–14] Photodynamic therapy (PDT) utilizes light to activate photosensitizers (PSs) to generate ROS, which induce apoptosis or necrosis in cancer cells, thereby achieving therapeutic effects.[7,15,16] Due to its minimally invasive nature, low side effects, and high biocompatibility, PDT has become one of the most promising alternative methods for tumor treatment. In this sense, PDT guided by PTI is believed to have certain advantages in tumor theranostics, and is a promising approach for achieving more precise image-guided treatment.

Organic phototheranostic agents usually have better biocompatibility, lower toxicity, higher structural diversity, higher cost-effectiveness and environmental friendliness, thus attracting increasing interest. To fulfill the task of developing high-performance organic phototheranostic agents, it is essential to understand excited-state energy dissipation mechanisms. When excited by light, the organic molecules would possibly undergo the following processes, which are (i) radiative dissipation, where the singlet excited state (S_1) directly radiates back to the ground state (S_0), which is known as fluorescence emission; (ii) non-radiative vibrational relaxation to S_0, namely

Key Laboratory for Advanced Materials, Joint International Research Laboratory of Precision Chemistry and Molecular Engineering, Feringa Nobel Prize Scientist Joint Research Center, School of Chemistry and Molecular Engineering, East China University of Science and Technology, 130 Meilong Road, Shanghai, 200237, China. E-mail: daisymeiju@ecust.edu.cn

† Electronic supplementary information (ESI) available: Experimental section, synthetic routes, details of synthesis/characterization, theoretical calculation method, ROS generating ability test, photothermal property measurements, fabrication and characterization of nanoparticles, and cellular and *in vivo* PDT, as well as the original spectra. See DOI: https://doi.org/10.1039/d5qm00094g

internal conversion, manifested in the thermal inactivation processes of photothermal therapy (PTT), photothermal imaging (PTI), and photoacoustic imaging (PAI); and (iii) the intersystem crossing (ISC) process, transitioning from S_1 to the lowest triplet state (T_1), primarily manifested in phosphorescence afterglow imaging and ROS-mediated PDT.[7,9,16–18] These three energy dissipation pathways are competitive. Therefore, it is feasible to suppress the energy dissipation pathway to fluorescence emission to increase the photo-induced heat generation and ROS production.[19,20]

The light exposure of PSs generates reactive oxygen species (ROS) types including superoxide radicals ($O_2^{\bullet-}$), hydroxyl radicals ($^{\bullet}OH$), singlet oxygen ($^1O_2$), *etc.*[21] According to the mechanism of ROS generation, the type I and type II ROS are produced by electron transfer and energy transfer, respectively.[4,7,21] In contrast to the type II PSs, the ROS generation of PSs *via* the type I mechanism does not rely on oxygen to produce free radical substances; thus their therapeutic performance is resistant to the hypoxic environment of the tumors.[22–27] So far, through various efforts such as reducing T_1 state energy and enhancing the electron transfer process by introducing highly electron-affinitive groups, building D–π–A structures, and so on, a number of type I PSs have been recently reported.[22,28] These PSs include but are not restricted to metal oxides,[29] carbon nanomaterials,[30] organic–inorganic hybrids (*e.g.*, metal–organic frameworks (MOFs)),[31] transition-metal complexes,[32,33] organic small molecules,[34,35] supramolecules,[36–38] and polymers.[39,40] Nevertheless, there is still an urgent demand for type I PSs, as most of the existing organic small-molecule PSs are primarily type II because of the lack of efficient design principles.[22,28,41–44]

In view of the merits of PTI and type I PSs,[18,22,28,45–55] herein we employ a molecular engineering strategy to construct a D–π–A system with the electron donor alternating between 4-methoxy-*N*-(4-methoxyphenyl)-*N*-phenylaniline and 9-ethyl-*N*,*N*-bis(4-methoxyphenyl)-9*H*-carbazol-2-amine, while the electron acceptor alternating between 1-ethylpyridin-1-ium and 1-ethylquinolin-1-ium (Scheme 1). Such D–π–A structures are designed to facilitate the ISC process and the subsequent electron transfer to result in prominent generation of hydroxyl radical and superoxide anion. As revealed by the theoretical calculations, the enlargement and partial flattening of the electron donor increase the π conjugation, which on the one hand red-shifts the emission and absorption wavelengths, and on the other hand suppresses the radiative decay of the excited state while boosting the production of heat and type I ROS.[18,22,28,45–52] The designed D–π–A conjugated organic molecules TPAPy, TPAQu, TPACzPy and TPACzQu were facilely synthesized. Among them, TPACzPy was chosen as a representative for the cellular and *in vivo* experiments. TPACzPy exhibited excellent type-I-dominant photosensitizing properties under white-light irradiation. The photothermal effect was successfully achieved under 660 nm-laser irradiation. Biocompatible TPACzPy NPs in which the TPACzPy molecules are encapsulated by F-127 were prepared *via* a nanoprecipitation method.[56] Due to their excellent photothermal properties, TPACzPy NPs can be used for tumor imaging in live mice. The *in vivo* therapeutic efficacy experiments

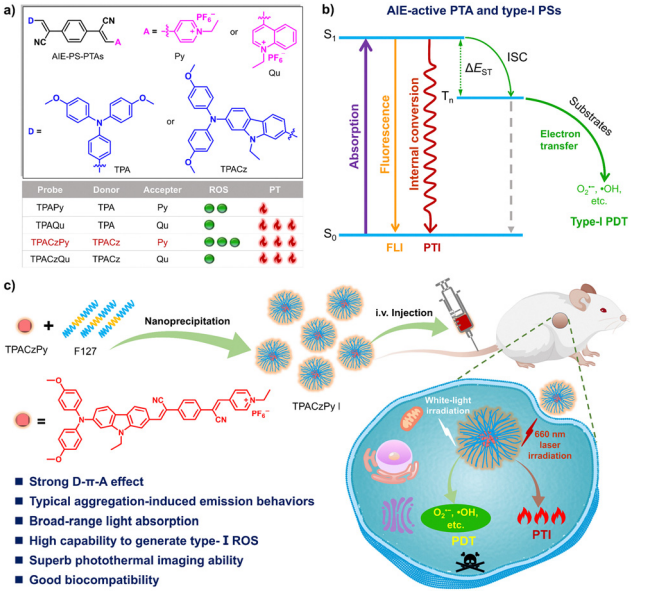

Scheme 1 (a) The molecular design, structures, and performances of AIE-active photosensitizers with photothermal effect (AIE-PS-PTAs). (b) The working mechanism of AIE-active photothermal agents (PTAs) and type-I photosensitizers (PSs). (c) A schematic illustration of the fabrication of TPACzPy nanoparticles and the photothermal imaging-guided PDT.

demonstrated that TPACzPy NPs not only inhibited tumor growth but also exhibited biological safety in mice. Therefore, this study serves as a prime example of how to adjust the energy dissipation mode to realize PTI-guided PDT.

Results and discussion

Molecular design, synthesis, and characterization

Four D–π–A structured compounds were constructed, featuring an asymmetric 2,2′-(1,4-phenylene)dipropionitrile backbone. The electron donor was either methoxy-modified triphenylamine or methoxy-decorated diphenylamine-carbazole, while the pyridinium (Py) and quinolinium (Qu) served as the electron acceptors. These combinations yielded the compounds TPAPy, TPAQu, TPACzPy, and TPACzQu, as depicted in Fig. 1a. The synthetic routes are detailed in Schemes S1 and S2, with the comprehensive structural characterization data provided in Fig. S1–S37 of the ESI.†

Theoretical calculations

The strong D–A interaction of these four compounds is supposed to facilitate intramolecular charge transfer (ICT), thereby reducing the energy bandgap, promoting the ISC process, achieving long-wavelength absorption and emission, and efficient ROS generation.

Such a design rationale was verified by the theoretical calculations. The energy gaps (E_g) between the highest occupied molecular orbitals (HOMOs) and the lowest unoccupied molecular orbitals (LUMOs) of TPAPy, TPAQu, TPACzPy, and TPACzQu are calculated to be as small as 1.19, 1.12, 0.64, and 0.59 eV, respectively (Fig. 1b). It is clear that the energy gap is greatly

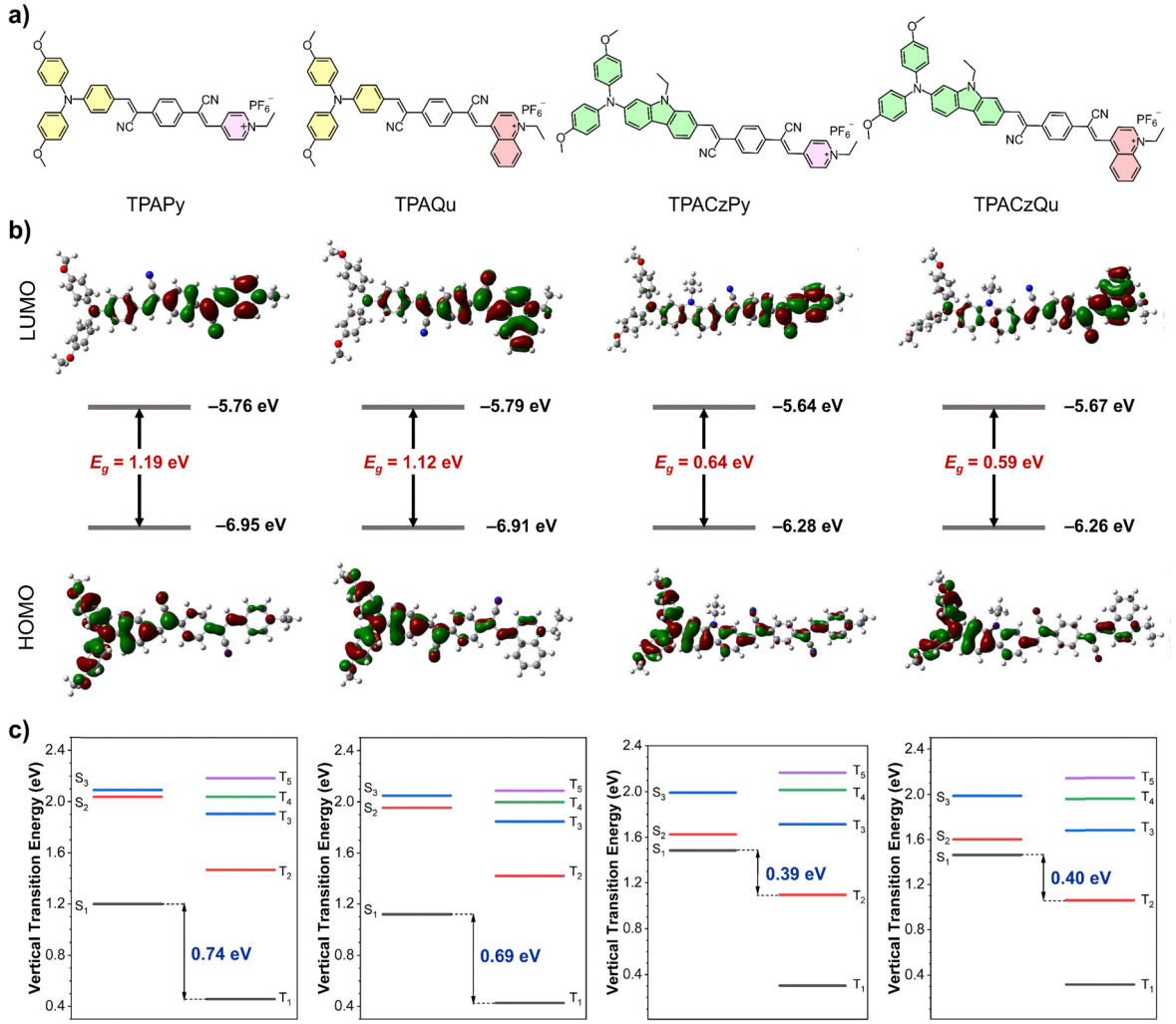

Fig. 1 (a) The molecular structures of TPAPy, TPAQu, TPAczPy, and TPACzQu. (b) Optimized geometries and molecular orbitals of the HOMO and LUMO levels. (c) Singlet (S)- and triplet (T)-state energy levels of TPAPy, TPAQu, TPAczPy, and TPACzQu.

affected by the electron donor, as the difference in the energy gap is 0.55 eV between TPAPy and TPACzPy, while that between TPAQu and TPACzQu is 0.53 eV. It might be because the introduction of electron-donating carbazole groups on the one hand extends the π-conjugation and on the other hand enhances the D–A interaction. Additionally, since the electron-withdrawing ability of Qu is relatively stronger than that of Py, the energy gaps of TPAQu and TPACzQu are slightly smaller than those of TPAPy and TPACzPy, respectively. Evident ICT could be observed as the electron clouds in the HOMO are mainly distributed on the triphenylamine or diphenylamine-carbazole, while the LUMO is primarily located on the electron-withdrawing group Py or Qu. It is shown that the HOMO and LUMO distributions of TPACzPy and TPACzQu are more significantly separated as compared to those of TPAPy and TPAQu.

To gain deeper insights into the electronic configurations and the characteristics of excited states, the ternary energy conversion of these four compounds was evaluated through time-dependent density functional theory (TD-DFT). Fig. 1c and Tables S1–S4 (ESI†) revealed that TPAPy, TPAQu, TPACzPy, and TPACzQu all display minimal energy gaps between the lowest singlet state (S_1) and the triplet state (T_n) ranging from 0.39 to 0.74 eV, suggesting a high likelihood of ISC processes. TPACzPy features a minimal ΔE_{ST} of 0.39 eV and a significant spatial separation between the HOMO and LUMO electron clouds, implying that its fluorescence channel might be reduced while efficiently generating ROS. Furthermore, as depicted in Fig. S38 (ESI†), the dihedral angles between the central benzene ring and the pyridinium or quinolinium rings of TPAPy, TPAQu, TPACzPy, and TPACzQu are 1.88°, 35.92°, 9.63°, and 32.5°, respectively. All these four compounds possess twisted molecular conformations, leading to a looser molecular packing in the aggregated state. Such a distorted 3D conformation is advantageous for promoting non-radiative decay pathways and enhancing photothermal performance.[57,58]

Photophysical property investigation

Solvatochromism and AIE characteristics. To explore the photophysical properties of these four compounds, we measured their UV-vis absorption and photoluminescence (PL)

spectra first in different solvents with various polarities. As shown in Fig. S39 (ESI†), these four compounds exhibit broad absorption bands in the range of 400–700 nm, which vary in different solvents. Notably, the absorption spectral shifts for TPAPy and TPACzPy are notably more significant, exhibiting a change of approximately 20 nm, compared to the less pronounced shifts observed for TPAQu and TPACzQu. In the PL spectra of TPAQu and TPACzQu, a noticeable red shift in the emission wavelength was observed with increasing solvent polarity (Fig. S40, ESI†). Moreover, the fluorescence spectra reveal that as the solvent polarity increases, all four compounds show substantial quenching behaviors, likely attributable to the ICT effect stemming from their D–A electronic structures. Hence, these four compounds exhibit solvatochromic properties. In dioxane, TPAPy, TPAQu, TPACzPy, and TPACzQu show maximum absorption peaks at 502, 408, 511, and 438 nm, respectively, with their absorption spectra extending up to about 700 nm. Correspondingly, their emission maxima are centered at 622, 579, 625, and 576 nm (Fig. 2a). The solid-state absorption spectra of these four compounds shown in Fig. S41 (ESI†) suggest the strong absorption across a broad wavelength range from 200 to 1000 nm. The broad and unstructured solid-state absorption profiles likely stem from the complex interplay of multiple solid-state effects including charge transfer, exciton coupling/delocalization, disordered packing, conformational diversity, and bandgap narrowing, which are associated with the flexible D–π–A structure. The AIE properties of these compounds were studied in the dimethyl sulfoxide (DMSO)/toluene mixtures with different fractions of toluene (Fig. S42 and S43, ESI†). As displayed in Fig. S43 (ESI†) and Fig. 2b, with the increase of the toluene fraction, all four compounds exhibit a significant enhancement in the fluorescence intensity, manifesting their typical AIE characteristics.

Photosensitizing and photothermal properties of the aggregates. Given that the photosensitizing properties are often enhanced by the AIE and ICT effects, we assessed the total ROS generation potential of the four AIE-active luminogens (AIEgens) using 2′,7′-dichlorodihydrofluorescein diacetate (DCFH-DA) as an indicator. As shown in Fig. 2c and Fig. S44 (ESI†), upon white-light irradiation, the DCFH solution containing TPAPy, TPAQu, TPACzPy, or TPACzQu displayed a markedly intensified fluorescence emission compared to both the blank group and the one containing commercially available photosensitizer Rose Bengal (RB). Notably, TPACzPy demonstrated the most significant increase in the fluorescence emission intensity, indicating that it has the highest ROS generation capability

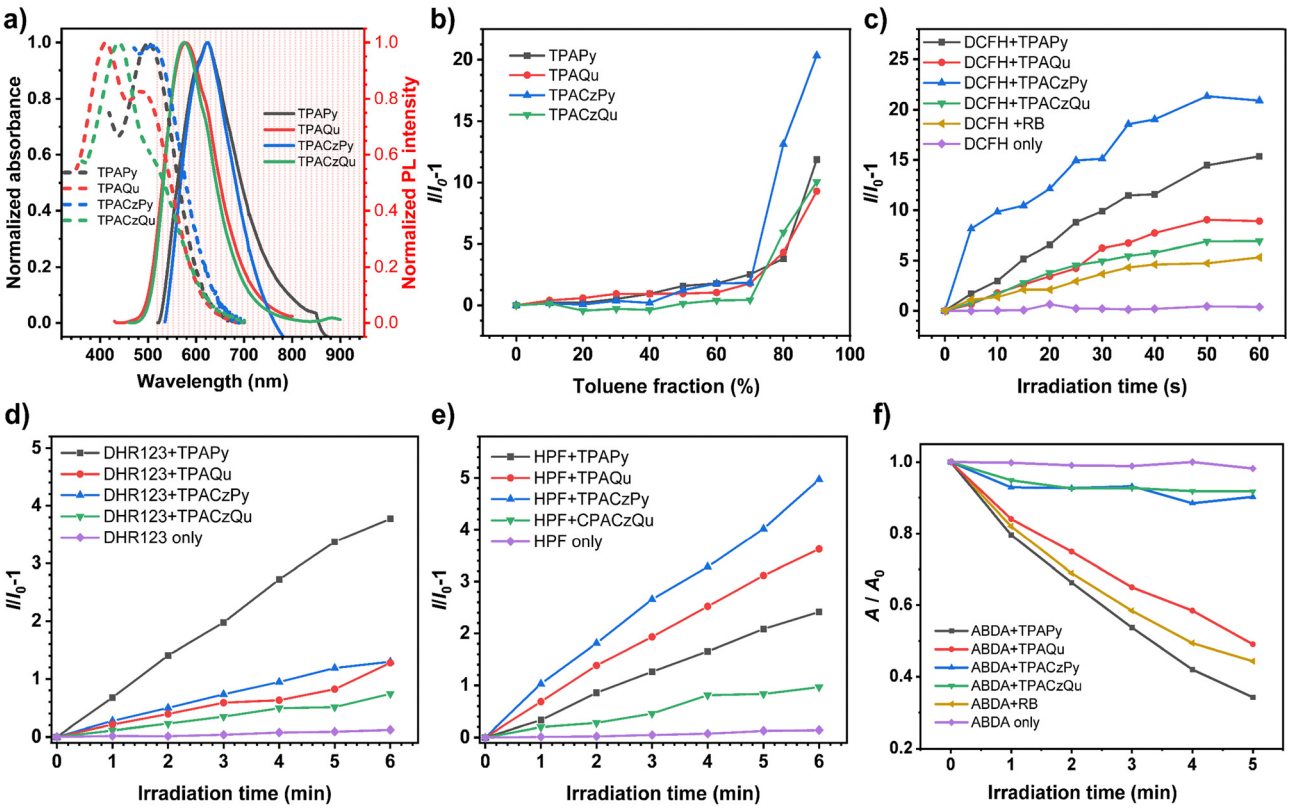

Fig. 2 (a) Normalized absorption spectra and normalized photoluminescence (PL) spectra of the compounds in 1,4-dioxane. TPAPy: λ_{ex} = 500 nm, TPAQu: λ_{ex} = 410 nm, TPACzPy: λ_{ex} = 515 nm, TPACzQu: λ_{ex} = 440 nm. (b) Plots of the relative emission intensity ($I/I_0 - 1$) of four compounds *versus* the toluene fraction of DMSO/toluene mixtures, where I_0 and I are their peak values of emission intensity in toluene and the DMSO/toluene mixture, respectively. Enhancement in the emission intensity of (c) DCFH, (d) DHR123, (e) HPF coexisting with TPAPy, TPAQu, TPACzPy, and TPACzQu under the white-light illumination for different time periods, respectively. DCFH: λ_{ex} = 488 nm, DHR 123: λ_{ex} = 490 nm, HPF: λ_{ex} = 480 nm. (f) The change in the UV-vis absorbance of ABDA coexisting with TPAPy, TPAQu, TPACzPy, and TPACzQu under white-light illumination for different time periods.

among the four AIEgens. It further confirms that the strength of the photosensitizing ability correlates positively with the intensity of the AIE and the ICT effects.

To determine the specific ROS generated by these four AIEgens, dihydrorhodamine 123 (DHR 123), hydroxyphenyl fluorescein (HPF), and 9,10-anthracenediyl-bis(methylene) dimalonic acid (ABDA) were utilized as indicators for the generation capability of a superoxide anion ($O_2^{\bullet -}$), a hydroxyl radical ($^{\bullet}OH$), and singlet oxygen ($^1O_2$), respectively (Fig. 2d–f and Fig. S45, S46, ESI†). Upon exposure to white-light irradiation, all four compounds exhibited remarkable generation of $O_2^{\bullet -}$ (Fig. 2d and Fig. S45a, d, S46a, d, ESI†) and $^{\bullet}OH$ (Fig. 2e and S45b, e, S46b, e, ESI†) when compared to the blank group. As evidenced in Fig. 2f and Fig. S45c, f, S46c, f (ESI†), the absorbance of ABDA decreased significantly over the irradiation time when coexisting with TPAPy and TPAQu, indicative of notable $^1O_2$ generation. In contrast, the absorbance of ABDA showed a minimal change in the presence of TPACzPy and TPACzQu, suggestive of a much lower generation of $^1O_2$ in these cases. These results collectively indicate that TPAPy and TPAQu generate a combination of type I and type II ROS, whereas TPACzPy and TPACzQu primarily produce type I ROS. Furthermore, the photothermal properties of these AIEgens were investigated by exposing them to a 660 nm laser and monitoring the temperature increase in the solid state as well as the heating–cooling cycles over five iterations (Fig. S47 and S48, ESI†). The results showed that the temperature of all four AIEgens in the solid form could exceed 100 °C within just 5 minutes even after five cycles, highlighting their considerable photothermal performance.

Photothermal properties of the nanoparticles (NPs). The above results revealed that TPAPy, TPAQu, TPACzPy, and TPACzQu, as AIEgens, possessed commendable photosensitizing and photothermal properties, demonstrating their high potential for application as phototheranostic agents. To improve the water dispersibility and biocompatibility of these AIEgens, we employed amphiphilic encapsulation matrices, specifically F127, to fabricate organic NPs through the nanoprecipitation method. Dynamic light scattering (DLS) measurements showed that the obtained TPACzPy NPs could disperse well in aqueous media, with an average hydrodynamic diameter of 71 nm (Fig. 3a). Transmission electron microscopy (TEM) observations revealed that the TPACzPy NPs exhibited a spherical and relatively uniform morphology. It is widely recognized that NPs with diameters between 10 and 100 nm possess a strong enhanced permeability and a retention (EPR) effect, facilitating their preferential accumulation at tumor sites, which is conducive to *in vivo* cancer treatment. To determine the concentration of the organic NPs encapsulated by F127, UV-vis absorption spectroscopy was performed at different concentrations of AIEgen, and the calibration curves for the organic NPs of different AIEgens were plotted

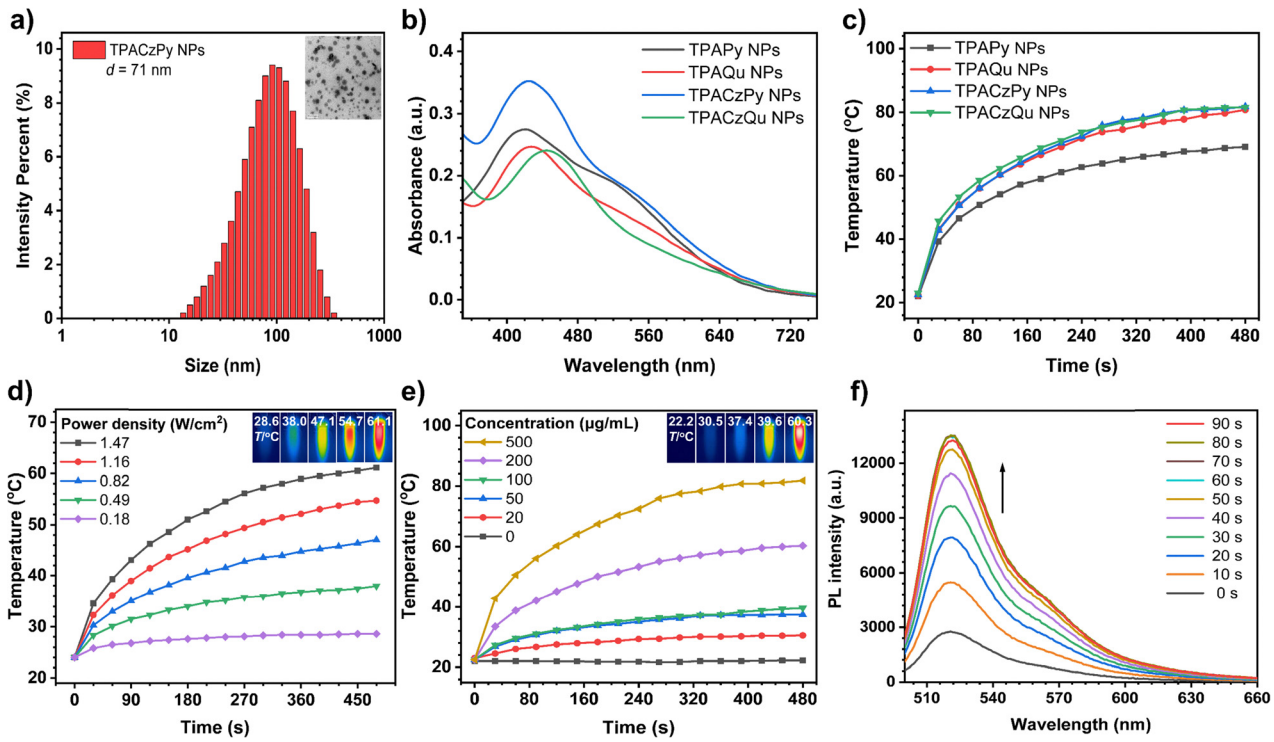

Fig. 3 (a) The dynamic light scattering (DLS) analysis results and scanning electron microscopy (SEM) images of the TPACzPy nanoparticles (NPs) in ultrapure water. (b) Absorption spectra of the NPs of these four AIEgens in ultrapure water. (c) The temperature variations of the AIE NPs in aqueous solution under 660 nm-laser irradiation at various time intervals (660 nm, 1.47 W cm^{-2}, 500 μg mL^{-1}). Photothermal behaviors of TPACzPy NPs at different (d) power densities and (e) concentrations. Insets: Actual photothermal effect diagrams of TPACzPy NPs at different power densities (inset in panel d) and concentrations (inset in panel e) after 8 minutes of irradiation with a 660 nm laser. (f) PL spectra of DCFH + TPACzPy NPs in the PBS buffer under the irradiation of white light for different time periods. λ_{ex} = 488 nm.

(Fig. S49 and S50, ESI†). The absorption spectra of the organic NPs displayed substantial broadening and red-shift as compared to the corresponding absorption peaks in solution (Fig. 3b). The organic NPs of these four AIEgens show a subtle but detectable absorption peak at 660 nm.

The photothermal performance of the organic NPs was further assessed using a 660 nm laser and an infrared thermal imaging camera, with the temperature rise curve recorded in eight minutes shown in Fig. 3c. It can be observed that the NPs of all these AIEgens exhibit excellent photothermal performance, with the temperature abruptly rising from about 20 to 80 °C (TPAQu, TPACzPy, and TPACzQu) or 60 °C (TPAPy) after being irradiated with a 660 nm-laser for 8 minutes. Moreover, the temperature rise curves depicted in Fig. 3d, e, and Fig. S51 (ESI†) indicate that there is a clear positive correlation between the photothermal behaviors of these AIE NPs and both their concentrations and the power density of the 660 nm laser. The infrared thermal images of the NPs at different concentrations and irradiated with different powder densities further confirmed their excellent photothermal imaging performance (insets in Fig. 3d, e, and Fig. S52, S53, ESI†). Notably, these organic NPs exhibit excellent photothermal stability under continuous irradiation of a 660 nm laser, with negligible changes in temperature observed after five cycles of heating and cooling (Fig. S54, ESI†). This indicates that these NPs have significant potential for long-term cancer treatment and diagnosis under laser irradiation. Additionally, the capacity of TPACzPy NPs to generate ROS upon photoexcitation was further validated in the PBS buffer, as illustrated in Fig. 3f. This result clearly demonstrates that the photosensitizing characteristics are preserved in the TPACzPy NPs. Bringing the above results together, it can be seen that TPACzPy stands out from the four

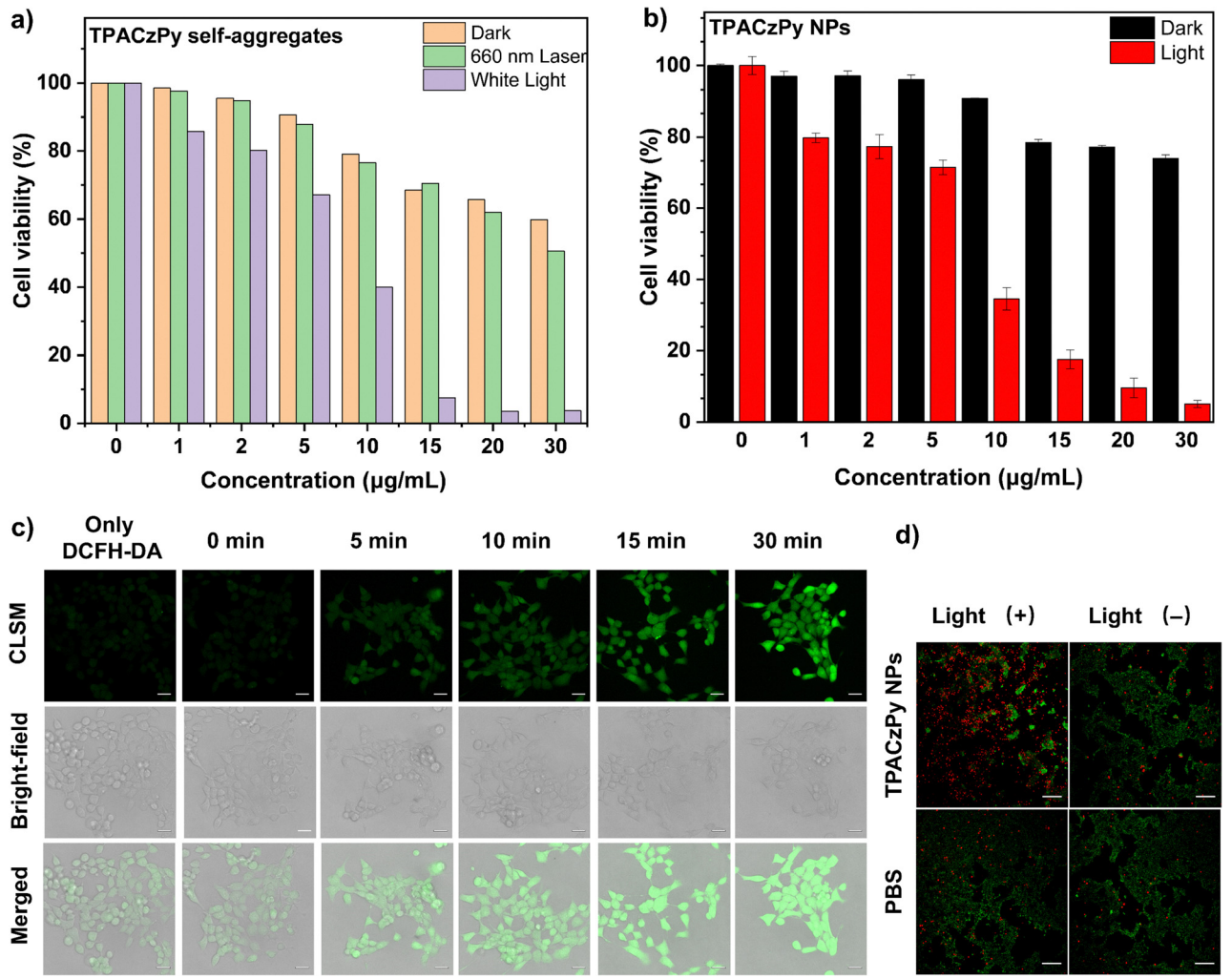

Fig. 4 (a) Viabilities of the 4T1 cells treated with various amounts of the self-aggregates of TPACzPy after the irradiation with white light or a 660 nm laser. (b) Viabilities of the 4T1 cells treated with various amounts of TPACzPy NPs after the irradiation of white light. (c) Intracellular detection of ROS generated by the TPACzPy NPs in the 4T1 cells after the irradiation with white light for different time periods with DCFH-DA as the indicator. λ_{ex} = 480 nm and λ_{em} = 490–550 nm. Scale bar = 20 μm. (d) Fluorescence images of the TPACzPy NPs (20 μM)-treated 4T1 cells with or without exposure to white-light irradiation, where the living and dead cells were stained using calcein-AM and PI, respectively. Calcein-AM: λ_{ex} = 495 nm, λ_{em} = 510–550 nm, PI: λ_{ex} = 535 nm, λ_{em} = 580–630 nm. Scale bar = 200 μm.

AIEgens with the longest absorption and emission wavelengths, the highest ROS generation ability, and robust photothermal performance, leading to its selection for further assessment as a representative phototheranostic agent.

In vitro evaluation of the phototheranostic effect of TPACzPy NPs

To optimize the conditions for phototheranostics, standard CCK-8 assays were conducted to measure the viability of 4T1 cells co-cultured with varying concentrations of self-aggregates of TPACzPy after irradiation with white light or 660 nm laser (Fig. 4a). It is evident that the white light-irradiated groups displayed superior cell-killing ability. Therefore, white light was selected as the light source for the following *in vitro* and *in vivo* experiments with TPACzPy NPs. As shown in Fig. 4b, the CCK-8 assay outcomes for 4T1 cells incubated with TPACzPy NPs in the absence of light suggested that TPACzPy NPs have low dark toxicity, with more than 90% cell viability maintained even after 12 hours of coculture in the dark. In sharp contrast, under the irradiation of white light, TPACzPy NPs show marked toxicity to 4T1 cells even at a concentration as low as 1 μg mL^{-1}, with the cell viability dropping to approximately 80%. As the concentration of TPACzPy NPs increases, there is a sharp decline in cell viability, demonstrating potent phototoxicity, with an IC_{50} estimated at around 6.5 μg mL^{-1}.

DCFH-DA was used to assess the intracellular ROS generation capability of TPACzPy NPs. As shown in Fig. 4c, after being incubated with TPACzPy NPs for 2 hours, the 4T1 cells show a green fluorescence signal which became intensified as time went by, indicating the existence of ROS. This observation not only highlights the ROS generation by TPACzPy NPs but also confirmed their photo-activated anti-tumor potential at the cellular level. To further specify the ROS produced by TPACzPy NPs, four different cell-permeable fluorescent ROS indicators, *i.e.*, DCFH-DA, DHR123, HPF, and singlet oxygen sensor green (SOSG), were used to monitor the intracellular production of total ROS, $O_2^{\bullet-}$, $^{\bullet}OH$, and $^1O_2$, respectively (Fig. S55, ESI†). Cells co-cultured with TPACzPy NPs and DCFH-DA, DHR123,

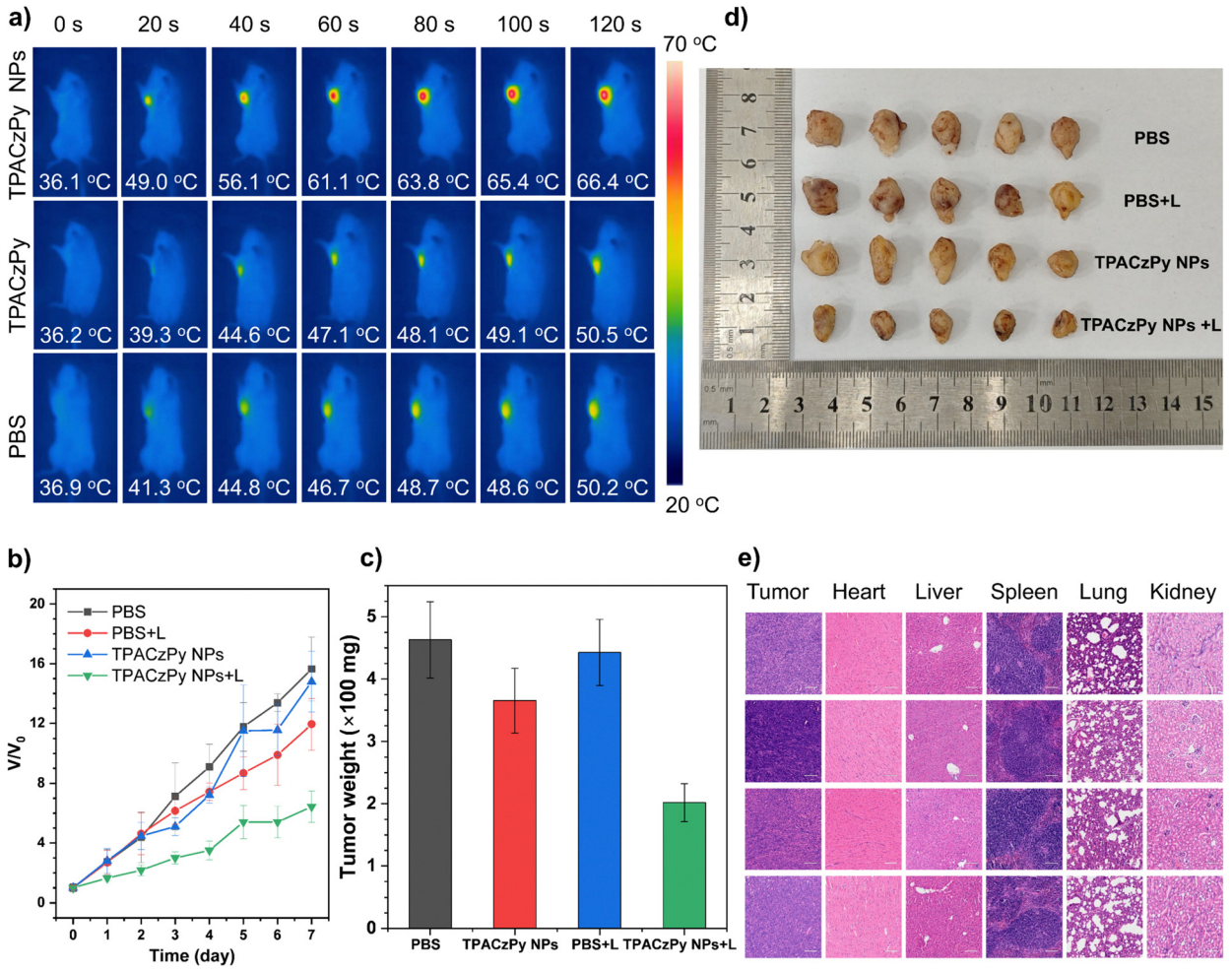

Fig. 5 (a) Thermal imaging of 4T1 tumor-bearing mice and the temperatures at corresponding tumor sites during continuous 660 nm laser irradiation at 20 h post-injection of TPACzPy NPs (mean ± SD, n = 3, *P < 0.001). The (b) relative tumor volume changes, (c) weights, and (d) photographs of the tumors excised from the mice after different treatments (mean ± SD, n = 5, *P < 0.001). (e) H&E staining of tumors, heart, liver, spleen, lungs, and kidneys of the mice after different treatments (from top to bottom: PBS, PBS + light, TPACzPy NPs, TPACzPy NPs + light).

or HPF gave a stronger green fluorescence signal after white-light irradiation as compared to the control groups, indicating that TPACzPy NPs can efficiently produce $O_2^{\bullet-}$ and $^{\bullet}OH$ in 4T1 cells under white-light illumination. Additionally, the 4T1 cells treated with TPACzPy NPs and SOSG showed no obvious fluorescence signal after white-light illumination. The results further confirmed that TPACzPy NPs function as type I photosensitizers. To visualize the photocytotoxicity of TPACzPy NPs, cell viabilities of 4T1 cells treated with TPACzPy NPs with and without white-light irradiation were evaluated using the AM-PI (calcein-propidium iodide) dual fluorescence staining method. Confocal laser scanning microscopy (CLSM) images of the 4T1 cells incubated with TPACzPy NPs and subjected to white-light irradiation showed a prominent red fluorescence signal which indicates the existence of dead cells (Fig. 4d). In contrast, the control groups mainly displayed distinct green fluorescence signals that suggest the presence of live cells. All the results validated that TPACzPy NPs exert an inhibitory effect on cancer cells under white-light irradiation.

In vivo evaluation of the phototheranostic effect of TPACzPy NPs

The *in vivo* photothermal imaging performance of TPACzPy NPs was evaluated when the 4T1 tumors in mice grew to about 200 mm^3. PBS, TPACzPy, or TPACzPy NPs were injected intravenously into the mice through the tail vein, and photothermal imaging was performed at the designated time points, capturing the thermal images and recording the real-time temperature accordingly (Fig. 5a and Fig. S56a, ESI†). As revealed by Fig. S56a (ESI†), the temperature difference between the TPACzPy NP group and the PBS group is the largest at 20 h post injection, which suggests the highest accumulation concentration of TPACzPy NPs in the tumor area at this time point. Thus, 20 hours after injection was determined as the optimal treatment time. As the TPACzPy NPs can passively target tumors due to the EPR effects while non-encapsulated TPACzPy can hardly be enriched in tumors, the temperature rise within two minutes of the TPACzPy NPs group is 30.3 °C, which is much higher than that in the TPACzPy and PBS groups (Fig. 5a). It demonstrates the *in vivo* photothermal imaging capacity of the TPACzPy NPs.

We further explored the *in vivo* photodynamic therapy capabilities of 4T1 tumor-bearing mice. When the tumor volume reached about 50 mm^3, the four groups of mice were injected with PBS or TPACzPy NPs intravenously. At 20 h after the injection, the tumors in mice of the PBS + light and TPACzPy NPs + light groups were irradiated with xenon lamps for 15 min. During the subsequent treatment period, the body weight, body temperature, and tumor volume of the mice at all groups were recorded daily. It can be observed that the tumor growth of mice in the TPACzPy NPs + light group is slower than that in the control groups (Fig. 5b). Moreover, the actual volume and weight of tumors dissected from mice in the TPACzPy NPs + light group were the smallest (Fig. 5c and d), demonstrating the inhibition effect exerted by TPACzPy NPs on the tumor growth. The biocompatibility of the TPACzPy NPs as well as the low photodamage were further evaluated. The hematoxylin and eosin (H&E) staining of the main organs *i.e.*, heart, liver, spleen, lungs and kidneys of mice in each group indicated no significant damage and inflammatory lesions in all the major organs (Fig. 5e). The blood biochemical analysis confirmed that TPACzPy NP treatment and xenon lamp irradiation imposed no significant effect on the liver and kidney functions (Fig. S56b and c, ESI†). Pictures of mice in each group during treatment displayed in Fig. S57 (ESI†) showed that all the light-treated groups exhibit negligible photodamage. It demonstrated that the TPACzPy NPs are highly biocompatible and capable of photodynamic inhibition of tumor growth.

Conclusions

To sum up, using a molecular engineering strategy, four D–π–A compounds were rationally designed and facilely constructed. These compounds feature AIE characteristics, photothermal and photosensitizing properties which are finely tuned by the modulation of the electron donor and acceptor. With the pronounced D–A effect promoting the ISC process as well as the bulky and partially flattened electron donor that extends the π-conjugation and enhances the nonradiative decay, TPACzPy shows the longest absorption and emission wavelengths, superior photothermal performance, and highest photosensitizing capability among the four AIE-active photothermal and photosensitizing agents. TPACzPy was thus selected as a representative for experiments at both the cellular and *in vivo* levels. A nanoplatform for PTI-guided cancer diagnosis and treatment was established by encapsulating the AIEgen into F-127 through nanoprecipitation. Cellular experiments demonstrated that TPACzPy NPs could effectively kill cancer cells by producing type I ROS under white-light illumination. *In vivo* experiments confirmed that TPACzPy NPs enabled high-resolution photothermal imaging-guided photodynamic therapy of cancer with excellent biocompatibility. This study not only offers promising candidates for PTI-guided PDT based on type-I photosensitizers but also exemplifies a molecular engineering approach to manipulate excited-state energy dissipation pathways for cancer phototheranostics.

Author contributions

X. Li: data curation, formal analysis, validation, investigation, visualization, and writing – original draft; S. Zhang: data curation, formal analysis, investigation, and visualization; P. Gu: data curation, formal analysis, and validation; X. Zhang: software, data curation, and validation; J. Mei: conceptualization, resources, supervision, funding acquisition, methodology, project administration, visualization, and writing – review and editing. All authors have given approval to the final version of the manuscript.

Data availability

The data that support the findings of this work are available from the corresponding author upon reasonable request.

Conflicts of interest

There are no conflicts to declare.

Acknowledgements

The authors appreciate the financial support from the National Natural Science Foundation of China (21788102, 22275055, 22025503, 22220102004, 21875064, and 21790361), the Shanghai Science and Technology Commission Basic Project Shanghai Natural Science Foundation (21ZR1417600), the Science and Technology Commission of Shanghai Municipality (24DX1400200), the Programme of Introducing Talents of Discipline to Universities (B16017), the Shanghai Science and Technology Committee (17520750100), the Science and Technology Commission of Shanghai Municipality (21JC1401700), and the Fundamental Research Funds for the Central Universities. This research was also supported by the "Oriental Talent Program Youth Project" (QNJY2024080). The authors acknowledge the support from the Research Center of Analysis and Test of East China University of Science and Technology for the help in characterization.

Notes and references

1 Y. Li, X. Li, X. Cao, J. Xu, X. Zhao and H. Lu, Single laser activated photodynamic/photothermal cancer therapy using a single mitochondria-targeted phototherapeutic agent with aggregation-induced emission characteristics, *Mater. Chem. Front.*, 2024, **8**, 2897.

2 Z. Fan, S. Wu, H. Deng, G. Li, L. Huang and H. Liu, Light-triggered nanozymes remodel the tumor hypoxic and immunosuppressive microenvironment for ferroptosis-enhanced antitumor immunity, *ACS Nano*, 2024, **18**, 12261.

3 D. Yan, Z. Zhang, J. Zhang, X. Li, Q. Wu, Y. Gui, J. Zhu, M. Kang, X. Chen, B. Z. Tang and D. Wang, An all-rounder for NIR-II phototheranostics: well-tailored 1064 nm-excitable molecule for photothermal combating of orthotopic breast cancer, *Angew. Chem., Int. Ed.*, 2024, **63**, 202401877.

4 K. Xue, X. Wang, D. Zhang, X. Wang, Y. Zhao, L. Yang, J. Deng and Z. Qi, Nanospheres of near-infrared aggregation-induced emission probes to target mitochondria to ablate tumors with reactive oxygen species generation under hypoxia, *ACS Appl. Nano Mater.*, 2023, **6**, 1448.

5 X. Yi, W. Zeng, C. Wang, Y. Chen, L. Zheng, Z. Zhu, X. Zhu, Y. Ke, X. He, Y. Kuang and Q. Huang, A step-by-step multiple stimuli-responsive metal-phenolic network prodrug nanoparticles for chemotherapy, *Nano Res.*, 2022, **15**, 1205.

6 B. Lu, Y. Huang, Z. Zhang, H. Quan and Y. Yao, Organic conjugated small molecules with donor–acceptor structures: design and application in the phototherapy of tumors, *Mater. Chem. Front.*, 2022, **6**, 2968.

7 M. Lan, S. Zhao, W. Liu, C. S. Lee, W. Zhang and P. Wang, Photosensitizers for photodynamic therapy, *Adv. Healthcare Mater.*, 2019, **8**, e1900132.

8 Q. Wang, Y. Dai, J. Xu, J. Cai, X. Niu, L. Zhang, R. Chen, Q. Shen, W. Huang and Q. Fan, All-in-one phototheranostics: single laser triggers NIR-II fluorescence/photoacoustic imaging guided photothermal/photodynamic/chemo combination therapy, *Adv. Funct. Mater.*, 2019, **29**, 1901480.

9 K. K. Ng and G. Zheng, Molecular interactions in organic nanoparticles for phototheranostic applications, *Chem. Rev.*, 2015, **115**, 11012.

10 X. Zhen, J. Zhang, J. Huang, C. Xie, Q. Miao and K. Pu, Macrotheranostic probe with disease-activated near-infrared fluorescence, photoacoustic, and photothermal signals for imaging-guided therapy, *Angew. Chem., Int. Ed.*, 2018, **57**, 7804.

11 J. Treekoon, K. Chansaenpak, G. Tumcharern, Z. S. Z. Zain, H. B. Lee, C. S. Kue and A. Kamkaew, Aza-BODIPY encapsulated polymeric nanoparticles as an effective nanodelivery system for photodynamic cancer treatment, *Mater. Chem. Front.*, 2021, **5**, 2283.

12 D. Zhao, Y. Deng, X. Jiang, Y. Bai, C. Qian, H. Shi and J. Wang, Advances in carbon dot based enhancement of photodynamic therapy of tumors, *ACS Appl. Bio Mater.*, 2024, **7**, 8149.

13 Z. Sun, H. Wen, Z. Zhang, W. Xu, M. Bao, H. Mo, X. Hua, J. Niu, J. Song, M. Kang, D. Wang and B. Z. Tang, Acceptor engineering-facilitated versatile AIEgen for mitochondria-targeted multimodal imaging-guided cancer photoimmunotherapy, *Biomaterials*, 2023, **301**, 122276.

14 X. Zhao, M. Sun, X. Cao, J. Xu, X. Li, X. Zhao and H. Lu, Near-infrared light-driving organic photothermal agents with an 88.9% photothermal conversion efficiency for image-guided synergistic phototherapy, *Adv. Healthcare Mater.*, 2024, **13**, 2400201.

15 J.-J. Hu, W. Jiang, L. Yuan, C. Duan, Q. Yuan, Z. Long, X. Lou and F. Xia, Recent advances in stimuli-responsive theranostic systems with aggregation-induced emission characteristics, *Aggregate*, 2021, **2**, 48.

16 J. Qi, H. Qu, Q. Liu and D. Ding, Gathering brings strength: how organic aggregates boost disease phototheranostics, *Aggregate*, 2021, **2**, 95.

17 P. De Bonfils, C. Sandoval-Altamirano, X. Moreau, P. Nun, A. D. Laurent, G. Gunther and V. Coeffard, Synthesis and photophysical characterizations of pyrroloquinolone photosensitizers for singlet oxygen production, *Photochem. Photobiol.*, 2023, **99**, 642.

18 C. Chen, X. Ni, H. W. Tian, Q. Liu, D. S. Guo and D. Ding, Calixarene-based supramolecular AIE dots with highly inhibited nonradiative decay and intersystem crossing for ultrasensitive fluorescence image-guided cancer surgery, *Angew. Chem., Int. Ed.*, 2020, **59**, 10008.

19 C. Liu, S. Zhang, J. Li, J. Wei, K. Müllen and M. Yin, A water-soluble, NIR-absorbing quaterrylenediimide chromophore

for photoacoustic imaging and efficient photothermal cancer therapy, *Angew. Chem., Int. Ed.*, 2019, **58**, 1638.
20 E. G. Kaye, K. Kailass, O. Sadovski and A. A. Beharry, A green-absorbing, red-fluorescent phenalenone-based photosensitizer as a theranostic agent for photodynamic therapy, *ACS Med. Chem. Lett.*, 2021, **12**, 1295.
21 R. Qu, X. Zhen and X. Jiang, Emerging designs of aggregation-induced emission agents for enhanced phototherapy applications, *CCS Chem.*, 2022, **4**, 401.
22 D. Chen, Q. Xu, W. Wang, J. Shao, W. Huang and X. Dong, Type I photosensitizers revitalizing photodynamic oncotherapy, *Small*, 2021, **17**, 2006742.
23 M.-Y. Wu, Y. Wang, L.-J. Wang, J.-L. Wang, F.-W. Xia and S. Feng, A novel furo[3,2-c]pyridine-based AIE photosensitizer for specific imaging and photodynamic ablation of Gram-positive bacteria, *Chem. Commun.*, 2022, **58**, 10392.
24 H. Wang, T. Qin, W. Wang, X. Zhou, F. Lin, G. Liang, Z. Yang, Z. Chi and B. Z. Tang, Selenium-containing type-I organic photosensitizers with dual reactive oxygen species of superoxide and hydroxyl radicals as switch-hitter for photodynamic therapy, *Adv. Sci.*, 2023, **10**, 2301902.
25 X. Han, Z. Zhou, K. Wang, Z. Zheng, S. E. Neumann, H. Zhang, T. Ma and O. M. Yaghi, Crystalline polyphenylene covalent organic frameworks, *J. Am. Chem. Soc.*, 2024, **146**, 89.
26 S. Ning, M. Lyu, D. Zhu, J. W. Y. Lam, Q. Huang, T. Zhang and B. Z. Tang, Type-I AIE photosensitizer loaded biomimetic system boosting cuproptosis to inhibit breast cancer metastasis and rechallenge, *ACS Nano*, 2023, **17**, 10206.
27 Y. He, J. Wan, Y. Yang, P. Yuan, C. Yang, Z. Wang and L. Zhang, Multifunctional polypyrrole-coated mesoporous TiO_2 nanocomposites for photothermal, sonodynamic, and chemotherapeutic treatments and dual-modal ultrasound/photoacoustic imaging of tumors, *Adv. Healthcare Mater.*, 2019, **8**, 1801254.
28 N. Ma, J. Wang, H. Tang, S. Wu, X. Liu, K. Chen, Y. Zhang and X. Yu, The current advances in design strategy (indirect strategy and direct strategy) for type-I photosensitizers, *Adv. Sci.*, 2025, **12**, 2413365.
29 J.-Y. Zhou, W.-J. Wang, C.-Y. Zhang, Y.-Y. Ling, X.-J. Hong, Q. Su, W.-G. Li, Z.-W. Mao, B. Cheng, C.-P. Tan and T. Wu, Ru(II)-modified TiO_2 nanoparticles for hypoxia-adaptive photo-immunotherapy of oral squamous cell carcinoma, *Biomaterials*, 2022, **289**, 121757.
30 Y. Zhang, H. Xia, M. Yang, H. Li, F. Shan, Y. Chen, X. Yue, Z. Wang and X. Yu, Carbon dots with two-photon fluorescence imaging for efficient synergistic trimodal therapy, *Chin. Chem. Lett.*, 2023, **34**, 108197.
31 J. Zhuang, S. Liu, B. Li, Z. Li, C. Wu, D. Xu, W. Pan, Z. Li, X. Liu and B. Liu, Electron transfer mediator modulates type II porphyrin-based metal-organic framework photosensitizers for type I photodynamic therapy, *Angew. Chem., Int. Ed.*, 2025, **64**, e202420643.
32 X. Su, W.-J. Wang, Q. Cao, H. Zhang, B. Liu, Y. Ling, X. Zhou and Z.-W. Mao, A carbonic anhydrase IX (CAIX)-anchored Rhenium(I) Photosensitizer evokes pyroptosis for enhanced anti-tumor immunity, *Angew. Chem., Int. Ed.*, 2022, **61**, e202115800.
33 N. Manav, A. Janaagal and I. Gupta, Unveiling new horizons: Exploring rhenium and iridium dipyrrinato complexes as luminescent theranostic agents for phototherapy, *Coord. Chem. Rev.*, 2024, **511**, 215798.
34 V. Juvekar, C. S. Lim, D. J. Lee, S. J. Park, G. O. Song, H. Kang and H. M. Kim, An azo dye for photodynamic therapy that is activated selectively by two-photon excitation, *Chem. Sci.*, 2021, **12**, 427.
35 S. Zeng, Y. Wang, C. Chen, H. Kim, X. Liu, M. Jiang, Y. Yu, Y. S. Kafuti, Q. Chen, J. Wang, X. Peng, H. Li and J. Yoon, An ER-targeted, viscosity-sensitive hemicyanine dye for the diagnosis of nonalcoholic fatty liver and photodynamic cancer therapy by activating pyroptosis pathway, *Angew. Chem., Int. Ed.*, 2024, **63**, e202316487.
36 W. Chen, Z. Wang, G. Hong, J. Du, F. Song and X. Peng, Self-assembly-integrated tumor targeting and electron transfer programming towards boosting tumor type I photodynamic therapy, *Chem. Sci.*, 2024, **15**, 10945.
37 P. He, M. Jia, L. Yang, H. Zhang, R. Chen, W. Yao, Y. Pan, Q. Fan, W. Hu and W. Huang, Zwitterionic photosensitizer-assembled nanocluster produces efficient photogenerated radicals via autoionization for superior antibacterial photodynamic therapy, *Adv. Mater.*, 2025, **37**, 2418978.
38 S. Yu, R.-X. Zhu, K.-K. Niu, N. Han, H. Liu and L.-B. Xing, Switchover from singlet oxygen to superoxide radical through a photoinduced two-step sequential energy transfer process, *Chem. Sci.*, 2024, **15**, 1870.
39 D. Chen, C. Liang, X. Qu, T. Zhang, X. Mou, Y. Cai, W. Wang, J. Shao and X. Dong, Metal-free polymer nanophotosensitizer actuates ferroptosis in starved cancer, *Biomaterials*, 2023, **292**, 121944.
40 J. Yu, J. Wu, J. Huang, C. Xu, M. Xu, C. Z. H. Koh, K. Pu and Y. Zhang, Hypoxia-tolerant polymeric photosensitizer prodrug for cancer photo-immunotherapy, *Nat. Commun.*, 2025, **16**, 153.
41 G. H. Luo, T. Z. Xu, X. Li, W. Jiang, Y. H. Duo and B. Z. Tang, Cellular organic-targeted smart AIEgens in tumor detection, imaging and therapeutics, *Coord. Chem. Rev.*, 2022, **462**, 214508.
42 M. Dirak, C. M. Yenici and S. Kolemen, Recent advances in organelle-targeted organic photosensitizers for efficient therapy, *Coord. Chem. Rev.*, 2024, **506**, 215710.
43 K.-X. Teng, W.-K. Chen, L.-Y. Niu, W.-H. Fang, G. Cui and Q.-Z. Yang, BODIPY-based photodynamic agents for exclusively generating superoxide radical over singlet oxygen, *Angew. Chem., Int. Ed.*, 2021, **60**, 19912.
44 S. Zhang, W. Yang, X. Lu, X. Zhang, Z. Pan, D.-H. Qu, D. Mei and J. Mei, Near-infrared AIEgens with high singlet-oxygen yields for mitochondria-specific imaging and antitumor photodynamic therapy, *Chem. Sci.*, 2023, **14**, 7076.
45 Z. Sheng, B. Guo, D. Hu, S. Xu, W. Wu, W. H. Liew, K. Yao, J. Jiang, C. Liu, H. Zheng and B. Liu, Bright aggregation-induced-emission dots for targeted synergetic NIR-II fluorescence and NIR-I photoacoustic imaging of orthotopic brain tumors, *Adv. Mater.*, 2018, **30**, 1800766.

46 S.-M. Wang, X. Lou, S. Xu, Z.-L. Song, T.-B. Ren, S.-Y. Huan, L. Yuan and X.-B. Zhang, Engineering of a novel D–A type fluorophore with hydrogen bond-induced enhanced emission property for sensitively detecting endogenous HOCl in living cells and tissues, *Anal. Bioanal. Chem.*, 2023, **415**, 4185.

47 L. Zhang, A. Yang, C. Ruan, B.-P. Jiang, X. Guo, H. Liang, W.-S. Kuo and X.-C. Shen, Copper-nitrogen-coordinated carbon dots: transformable phototheranostics from precise PTT/PDT to post-treatment imaging-guided PDT for residual tumor cells, *ACS Appl. Mater. Interfaces*, 2023, **15**, 3253–3265.

48 Y. Wan, Y. Gao, W.-C. Wei, K.-W. Lee, J.-H. Tan, C.-Y. Chen, H. Chen, S. Li, K.-T. Wong and C.-S. Lee, Facilely achieving near-infrared-II J-aggregates through molecular bending on a donor–acceptor fluorophore for high-performance tumor phototheranostics, *ACS Nano*, 2024, **18**, 27949.

49 H. Tang, N. Ma, X. Liu, S. Wu, H. Li, K. Chen, Y. Jiang, Y. Zhang, Z. Wang and X. Yu, A heterocyclic strategy for regulating the proportion of type I and type II photodynamic therapy, *Mater. Chem. Front.*, 2024, **8**, 2866.

50 L. Feng, C. Li, L. Liu, Z. Wang, Z. Chen, J. Yu, W. Ji, G. Jiang, P. Zhang, J. Wang and B. Z. Tang, Acceptor planarization and donor rotation: a facile strategy for realizing synergistic cancer phototherapy via type I PDT and PTT, *ACS Nano*, 2022, **16**, 4162.

51 X. Hu, Q. Jia, Q. Fang, C. Song, R. Zhang, Y. Liang, Z. Yang, J. Wu, B. Li, T. Zhao, D. Zhao and Z. Wang, Synchronously manipulating the D–A interaction and planarity in semiconducting polymers to achieve 84.7% photothermal conversion efficiency for NIR-II imaging-guided tumor therapy, *Adv. Funct. Mater.*, 2024, **34**, 2407100.

52 B. Lu, H. Quan, Z. Zhang, T. Li, J. Wang, Y. Ding, Y. Wang, X. Zhan and Y. Yao, End group nonplanarization enhances phototherapy efficacy of A–D–A fused-ring photosensitizer for tumor phototherapy, *Nano Lett.*, 2023, **23**, 2831.

53 X. Yang, X. Wang, X. Zhang, J. Zhang, J. W. Y. Lam, H. Sun, J. Yang, Y. Liang and B. Z. Tang, Donor–acceptor modulating of ionic AIE photosensitizers for enhanced ROS generation and NIR-II emission, *Adv. Mater.*, 2024, **36**, 2402182.

54 S. Li, X. Jin, Z. Zhang, J. Li and J. Hua, An AIE-active type I photosensitizer based on N,N′-diphenyl-dihydrophenazine for high-performance photodynamic therapy under hypoxia, *Mater. Chem. Front.*, 2023, **7**, 3738.

55 Y. Yu, S. Wu, L. Zhang, S. Xu, C. Dai, S. Gan, G. Xie, G. Feng and B. Z. Tang, Cationization to boost both type I and type II ROS generation for photodynamic therapy, *Biomaterials*, 2022, **280**, 121255.

56 K. Wen, H. Tan, Q. Peng, H. Chen, H. Ma, L. Wang, A. Peng, Q. Shi, X. Cai and H. Huang, Achieving efficient NIR-II type-I photosensitizers for photodynamic/photothermal therapy upon regulating chalcogen elements, *Adv. Mater.*, 2022, **34**, 2108146.

57 J. Chen, K. Wen, H. Chen, S. Jiang, X. Wu, L. Lv, A. Peng, S. Zhang and H. Huang, Achieving high-performance photothermal and photodynamic effects upon combining D–A structure and nonplanar conformation, *Small*, 2020, **16**, 2000909.

58 Z. Wang, L. Huang, Y. Yan, A. M. El-Zohry, A. Toffoletti, J. Zhao, A. Barbon, B. Dick, O. F. Mohammed and G. Han, Elucidation of the intersystem crossing mechanism in a helical BODIPY for low-dose photodynamic therapy, *Angew. Chem., Int. Ed.*, 2020, **59**, 16114.

